Label-free imaging of macrophage phenotypes and phagocytic activity in the human dermis *in vivo* using two-photon excited FLIM

M. Kröger[1], J. Scheffel[1], E. A. Shirshin[2], J. Schleusener[1], M. C. Meinke[1], J. Lademann[1], M. Maurer[1], M. E. Darvin[1]*

[1] Charité – Universitätsmedizin Berlin, corporate member of Freie Universität Berlin, Humboldt-Universität zu Berlin, and Berlin Institute of Health, Department of Dermatology, Venerology and Allergology, Charitéplatz 1, 10117 Berlin, Germany
[2] Lomonosov Moscow State University, Faculty of Physics, 119991, Leninskie gory 1/2, Moscow, Russia

* Corresponding author: Maxim E. Darvin
 E-mail: maxim.darvin@charite.de

Abstract

Macrophages (MΦs) are important immune effector cells that promote (M1 MΦs) or inhibit (M2 MΦs) inflammation and are involved in numerous physiological and pathogenic immune responses. Their precise role and relevance, however, is not fully understood because of the lack of non-invasive quantification methods. Here, we show that two-photon excited fluorescence lifetime imaging (TPE-FLIM), a label-free non-invasive method, can visualize MΦs in human dermis *in vivo*. We demonstrate *in vitro* that human dermal MΦs exhibit specific TPE-FLIM properties that distinguish them from the main components of the extracellular matrix and other dermal cells. We visualized MΦs, their phenotypes and phagocytosis in the skin of healthy individuals *in vivo* using TPE-FLIM. Additionally, machine learning identified M1 and M2 MΦs with a sensitivity of 0.88±0.04 and 0.82±0.03 and a specificity of 0.89±0.03 and 0.90±0.03, respectively. In clinical research, TPE-FLIM can advance the understanding of the role of MΦs in health and disease.

Introduction

Macrophages (MΦs) are important immune effector cells in organs and tissues that act as border junctions to environments such as the gut, the airways, and the skin (Elhelu, 1983). Skin MΦs (Dong et al., 2016; Estandarte et al., 2016; Ryter, 1985) originate from circulating monocytes (Geissmann et al., 2010; Gordon and Taylor, 2005) via the same infiltration route into the dermis as monocyte-derived dendritic cells (Schmid and Harris, 2014) (Fig. 1a) and are mainly located in the papillary and reticular dermis in close proximity to blood vessels (Weber-Matthiesen and Sterry, 1990) (Figs. 1b-d). It has been known for more than 30 years that skin MΦs are abundant and heterogeneous, based on their morphology, localization and staining properties (Weber-Matthiesen and Sterry, 1990). More recently, skin MΦs have been classified based on their function, and they fall into two phenotypes referred to as inflammation-promoting M1 MΦs (classically activated) and anti-inflammatory M2 MΦs (alternatively activated) (Duque and Descoteaux, 2014) (Fig. 1a). M1 MΦs are activated by viral and bacterial infection (Benoit et al., 2008; Ferrer et al., 2019; Malmgaard et al., 2004), interferon-γ, lipopolysaccharide (LPS), and tumor necrosis factor (TNF), which is known as the classical activation pathway (Li and Liu, 2018). M2 MΦs are alternatively activated in response to IL-4, IL-13 and IL-33 (Furukawa et al., 2017; Sica and Mantovani, 2012).
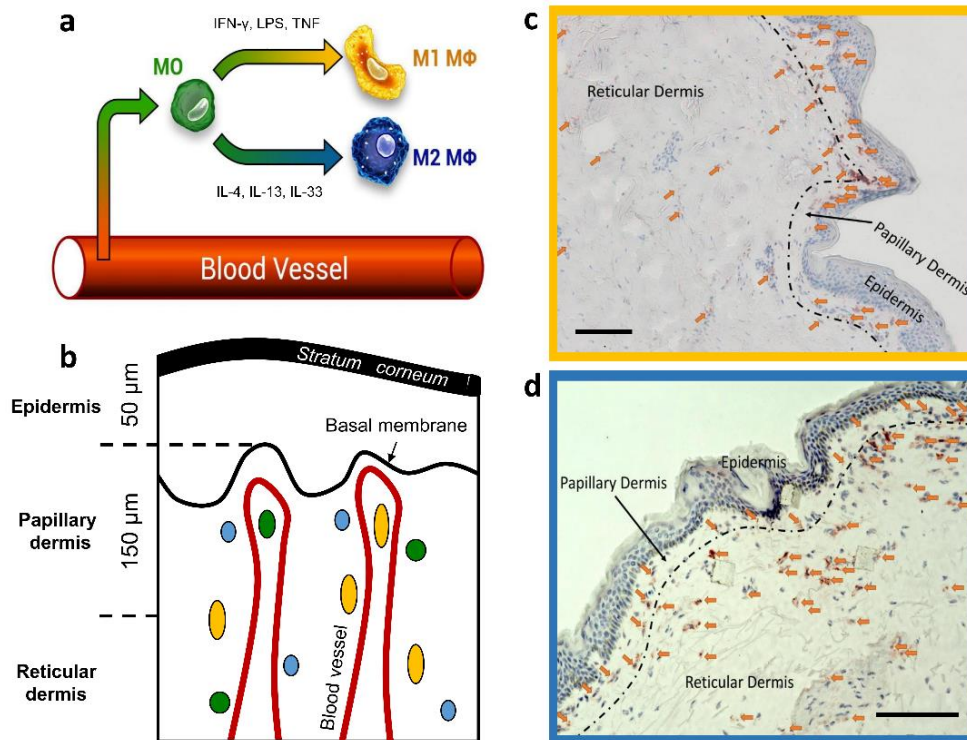
Figure 1. Dermal monocyte skin infiltration and CD68 stained M1 and CD163 stained M2 MΦs distribution in excised human skin. Schematic illustration of monocyte (MO) (green) infiltration into tissues and macrophage (MΦ)-polarization into M1 MΦs (yellow) via IFN-γ, LPS and TNF and M2 MΦs (blue) via IL-4, IL-13 and IL-33 (a). Schematic of skin with exemplary locations of monocytes (green), M1 MΦs (yellow) and M2 MΦs (blue) (b). Density of M1 MΦs (marked with arrows) stained with CD68 (c) and M2 MΦs (marked with arrows) stained with CD163 (d) in 10 µm thick cryo-section. Scale bar 100 µm. Recently, this paradigm has been challenged, as many signals modulate MΦ functions, resulting in a continuum of states between the M1 and M2 phenotypes(Mendoza-Coronel and Ortega, 2017; Murray et al., 2014). However, for simplicity, the terms M1 and M2 MΦs are used here.

Skin M1 MΦs are held to contribute to dermal innate immunity and homeostasis. This is supported by reports that M1 MΦs can phagocyte objects up to 20 µm in size (Morhenn et al., 2002), promote skin inflammatory and immune responses (Remmerie and Scott, 2018; Theret et al., 2019; Yanez et al., 2017), and produce nitric oxide and other reactive oxygen species (ROS) (Forman and Torres, 2001; Rendra et al., 2019). Skin M2 MΦs, on the other hand, are thought to promote dermal repair, healing and regeneration, for example by contributing to the formation of the extracellular matrix (Ploeger et al., 2013).

The precise role of skin MΦs and their M1 and M2 phenotypes in health and disease remains to be elucidated. Efforts to do so include their quantification in healthy human skin and in lesional and non-lesional skin of patients with skin diseases. Currently, the most common approach is to obtain skin biopsies and to visualise MΦs by immunohistochemistry. Skin biopsies, however, come with several important limitations, which include scarring, the risk of infection and bleeding, and artificial findings caused by the use of local anesthesia. Also, histopathological analyses of skin biopsies are not well suited for characterizing MΦ functions such as phagocytosis and for long term monitoring of MΦ distribution in the skin.

Fluorescence lifetime imaging (FLIM) employs NAD(P)H and fluorescence decay parameters of cellular compartments as specific indicators of cell types and phenotypes (Alfonso-García et al., 2016; Heaster et al., 2021). Combined with two-photon tomography, two-photon excited fluorescence lifetime imaging (TPE-FLIM) allows for label-free and non-invasive imaging of dermal cells. For instance, TPE-FLIM allows for *in vitro* imaging of mast cells, fibroblasts, neutrophils, and dendritic cells and *in vivo* imaging of mast cells in human skin (Kröger et al., 2020). Whether or not TPE-FLIM can be used to visualise human skin MΦs, their M1 and M2 phenotypes, and their functions, is currently unknown. There are, however, several independent lines of evidence that support this approach: First, previous studies have shown that TPE-FLIM can distinguish MΦs from other dermal cells and extracellular matrix (ECM), without prior labelling (Kröger et al., 2020). Second, the capillaries of the papillary dermis, which often are in a close proximity with MΦs, show distinct TPE-FLIM signatures and are readily visualised (Shirshin et al., 2017). Third, M1 and M2 MΦs come with unique cytokine patterns, and the TPE-FLIM signatures of these cytokines and patterns could help to tell the two phenotypes apart. Finally, TPE-FLIM can distinguish between functional states of dermal cells, e.g. resting and activated mast cells *in vivo*, MΦs *ex vivo* (Kröger et al., 2020) and T-cell activation *in vitro* (Walsh et al., 2021) may, therefore, potentially allow for monitoring MΦ functions *in vivo* (Szulczewski et al., 2016). Taken together, the morphological features of skin MΦs, their localization in the skin, and the expected differences in fluorescence decay parameters between MΦ phenotypes as well as between other dermal cells, make TPE-FLIM a promising strategy for their detection (Yakimov et al., 2019).

Here, we first investigated human skin MΦs, *in vitro,* for their TPE-FLIM properties and how these differ from those of the main components of the ECM and other dermal cells such as fibroblasts, mast cells, and dendritic cells. We then applied the identified MΦ TPE-FLIM signatures to investigate MΦs and their phenotypes in human skin biopsies, combined with traditional immunohistochemistry-based visualization. Finally, we used TPE-FLIM *in vivo* in humans to study skin MΦs, their phenotypes and functions, and we developed, tested, and characterised TPE-FLIM signature-based machine learning algorithms for the detection of skin MΦs.

Results

In vitro monocyte-derived M1 and M2 MΦs show distinct TPE-FLIM parameters

The TPE-FLIM images of monocytes isolated from human peripheral blood mononuclear cells (PBMC) showed a round morphology (diameter of up to 10 µm) with a barely visible nucleus, homogeneously distributed cell content, and regular borders with no membrane extensions (Fig. S1). MΦs differentiated from PBMC and polarised towards M1 MΦs with interferon-γ (IFN-γ; $n=21$) and towards M2 MΦs with interleukin-4 (IL-4; $n=27$) were similar in size, ranging from 10–12 µm (Fig. 2a, 2b and 2c). M1 and M2 MΦs showed comparable overall TPE-AF intensities, but they differed significantly in several other features. M1 MΦs also showed numerous bright spots (typical size is 2–3 µm), likely vacuoles and mitochondria, had less visible borders, and exhibited higher TPE-AF intensity than M2 MΦs. In contrast, M2 MΦs were characterised by distinct borders with filopodia (Fig. 2b; Fig. S2), which were rarely seen in M1 MΦs (Fig. 2a).
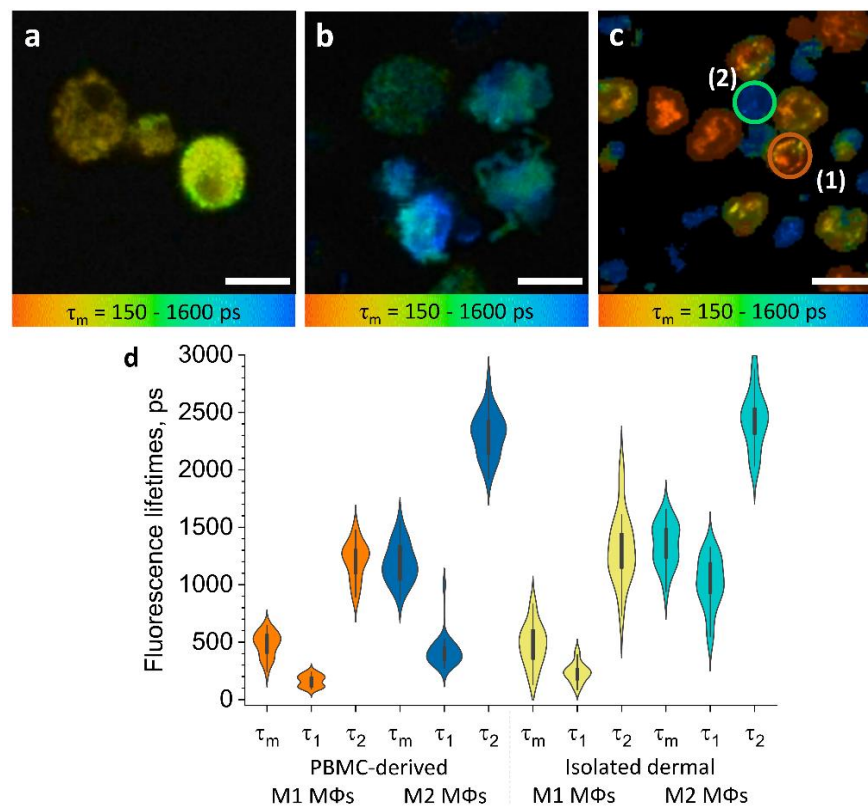

Figure 2. MΦs polarised from PBMC and isolated dermal MΦs show distinct TPE-FLIM signatures. TPE-FLIM τ_m images (mean fluorescence lifetime τ_m in the 150–1600 ps range) of monocyte-derived M1-polarised (IFN-γ) MΦs (a), monocyte-derived M2-polarised (IL-4) MΦs (b), and isolated human dermal M1 MΦs (1) and M2 MΦs (2) (c). Scale bar: 10 µm. The distribution of TPE-FLIM parameters τ_1, τ_2 and τ_m for monocyte-derived M1-polarised MΦs ($n=21$, orange), M2-polarised MΦs ($n=27$, dark blue), and isolated dermal M1 MΦs ($n=34$, yellow), M2 MΦs ($n=28$, light blue) (d). The boxplot represents 25–75% of the values.

M1 and M2 MΦs also differed in their TPE-FLIM parameters τ_1, τ_2, and τ_m (Fig. 2d). TPE-AF decay times were significantly shorter in M1 MΦs ($n=21$) than in M2 MΦs ($n=27$; $p<0.05$), and both MΦs differed significantly, in their TPE-FLIM parameters, from monocytes ($n=15$; $p<0.05$; Table 1).

IgG stimulation of IgG immune complex-sensitised M1 and M2 MΦs resulted in the release of inflammatory mediators, but did not lead to significant changes or reveal additional differences in TPE-FLIM parameters 2 and 5 days after differentiation of PBMC into MΦs (data not shown). Taken together, these findings indicate that monocyte-derived M1 MΦs and M2 MΦs can be identified and distinguished *in vitro* by their distinct TPE-FLIM signatures.

MΦs isolated from periocular skin show TPE-FLIM parameters that are similar to those of in vitro monocyte-derived M1 MΦs or M2 MΦs

Human MΦs isolated from periocular dermal tissue and analysed by immunohistochemistry were irregularly shaped, with poorly defined borders, 8–10 µm in size, pericentral nuclei of 5–6 µm diameter with low fluorescence intensity, heterogeneously and irregularly distributed cellular content, and they exhibited a bright fluorescence multi-vacuolated cytoplasm with ≈1 µm diameter small bright spots, presumably related to mitochondria and/or vacuoles (Fig. 2c). Based on their TPE-FLIM parameters, dermal MΦs fell into two significantly different groups (Fig. 2d): group 1 (n=34), with stronger TPE-AF intensity (≈3,000±500 photons/mW) and shorter lifetimes, and group 2 (n=28), with a weaker TPE-AF intensity (≈800±200 photons/mW) with longer lifetimes (Fig. 2c; Fig. S3). The profiles of dermal MΦs in group 1 and 2 were similar to those of monocyte-derived M1 MΦs and M2 MΦs, respectively (Fig. 2d; Table 1). The biggest differences between group 1 / M1 MΦs and group 2 / M2 MΦs were shorter τ_1 and τ_m as well as larger size (10.9±0.6 µm) in the former as compared to the latter (9.8±1.2 µm; p<0.05; Fig. 2c and 2d; Table 1). This suggests that human skin MΦs, based on their *in vitro* TPE-FLIM signatures, can be assigned to one of two phenotypes, where the first is similar to that of monocyte-derived M1 MΦs and the second is similar to that of monocyte-derived M2 MΦs.

Table 1. TPE-FLIM parameters for for investigated dermal and epidermal cells. TPE-FLIM parameters τ_1, τ_2, τ_m, a_1/a_2 and TPE-AF intensity of monocyte-derived M1 and M2 MΦs; dermal M1 and M2 MΦs isolated from the skin measured *in vitro*; M1 (CD68) and M2 (CD163) MΦs measured *ex vivo* in human skin cryo-sections; M1 and M2 MΦs observed on the forearm of healthy volunteers *in vivo*; monocytes; resting and activated human skin mast cells; dendritic cells; fibroblasts and neutrophils *in vitro*.

		Number of cells	τ_m in ps	τ_1 in ps	τ_2 in ps	a_1/a_2	TPE-AF intensity, photons /mW
in vitro	**Monocyte-derived M1-polarised MΦs**	21	479±106	163±50	1,209±161	2.4±0.6	600±100
in vitro	**Monocyte-derived M2-polarised MΦs**	27	1,185±170	417±134	2,305±194	2.3±0.5	500±100
in vitro	**M1 isolated dermal MΦs**	34	461±175	225±84	1,289±278	4.8±3.4	3,000±500
in vitro	**M2 isolated dermal MΦs**	28	1,281±155	807±250	2,352±229	2.2±1.1	800±200

ex vivo	**M1 MΦs (CD68)**	8	458±50	190±38	1,504±133	4.1±0.7	3,000±500
ex vivo	**M2 MΦs (CD163)**	12	1,369±201	498±129	2,267±155	1.1±0.4	700±300
in vivo	**M1 MΦs**	35	477±105	196±40	1,698±172	5.0±2.8	686±165
in vivo	**Phagocytosing M1 MΦs**	2	195±44	105±10	1,272±89	14.7±4.5	1,100±150
in vivo	**M2 MΦs**	25	1,407±60	442±54	2,458±90	1.2±0.2	360±155
in vitro	**PBMC-derived monocytes**	15	989±111	491±130	2,025±301	1.8±0.5	700±130
in vitro	**Resting mast cells**	43	1,248±287	533±266	2,289±317	1.5±0.5	1,300±400
in vitro	**Activated mast cells**	13	862±268	288±130	1,920±287	2.5±2.0	900±200
in vitro	**Dendritic cells**	14	1,265±180	434±188	2,578±328	1.6±0.2	538±258
in vitro	**Fibroblasts**	6	921±81	429±51	1,983±137	0.5±0.1	469±137
in vitro	**Neutrophils**	21	1,074±109	714±250	1,795±600	1.5±0.5	500±115

162

163

TPE-FLIM can distinguish between MΦs and other cells

To prove that the recorded TPE-FLIM signatures are unique for M1- and M2-polarized MΦs (Fig. 2), we performed TPE-FLIM measurements of other dermal cells *in vitro*, such as mast cells, dendritic cells, fibroblasts, monocytes and neutrophils. Their TPE-FLIM parameters, summarised in Table 1, are markedly different from those of the established signatures of M1- and M2-polarized MΦs. Thus, in addition to size, morphology, and internal vacuole structure, M1- and M2-polarized MΦs can be distinguished, from each other and other cells, by distinct TPE-FLIM parameters, a prerequisite for the visualization of skin MΦs *ex vivo* and *in vivo*. Table 1 is an extension of the results shown in Kröger *et al.*(Kröger et al., 2020)

Immunohistochemistry confirms TPE-FLIM detection of M1 and M2 MΦs in human skin ex vivo

To test if the TPE-FLIM signatures established *in vitro* identify M1- and M2-polarized MΦs in human skin, we sequentially analyzed dermal biopsies by TPE-FLIM and conventional immunohistochemistry. The application of *in vitro* MΦ signatures to TPE-FLIM analyses of 13 human skin biopsy cryo-sections identified two distinct cell populations: The first showed a short mean fluorescence lifetime τ_m and high TPE-AF intensity, a feature of M1 MΦs (Table 1, Fig. 2d, Fig. 3a); the second population showed longer τ_m and significantly lower TPE-AF intensity, typical for M2 MΦs (Table 1, Fig. 2d, Fig. 3c). CD68-staining for M1 MΦs and CD163-staining for M2 MΦs confirmed that short τ_m cells with high TPE-AF intensity were, indeed, M1 MΦs (Fig. 3b) and that cells with longer τ_1, τ_2, τ_m with low TPE-AF intensity were, indeed, M2 MΦs (Fig. 3d, Fig. S4, Table 1).
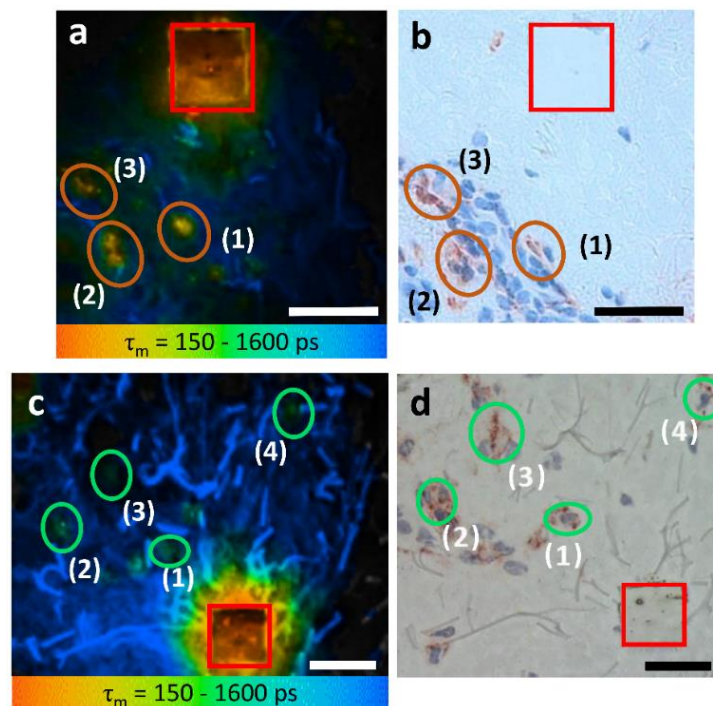

Figure 3. M1 and M2 MΦs *ex vivo* verified using TPE-FLIM parameters and immunohistochemistry-based bright field microscopy. Side by side comparison of TPE-FLIM τ_m image (mean fluorescence lifetime τ_m in the 150–1,600 ps range), which were measured label-free and then stained with CD68-antibody for M1 MΦs (a), and CD163-antibody for M2 MΦs (c) and corresponding bright field microscopic images (b) and (d). The excitation wavelength is 760 nm and laser power is 4 mW (a) and 2 mW (c). The M1 and M2 MΦs are marked with ellipses in (a,b) and in (c,d), respectively. The laser-burned labels (28 µm×28 µm) are marked in red. The suspected (a, c) and staining-proved (b, d) MΦs are marked with number (1, 2, 3 and 4). More M2 MΦs are observed in (d) compared to (c) due to the staining and visualization of the entire biopsy volume in (d) and limited imaging plane of the two-photon tomograph (1.2–2.0 µm) in (c). Images have been rotated and zoomed to match their orientation and size. Scale bar: 30 µm.

CD68-positive dermal M1 MΦs showed a heterogeneous appearance, ranging from flat and spindle shaped vessel lining to big intravascular with irregular borders and an irregular nucleus (Fig. 3b). The TPE-FLIM image of CD163-positive M2 MΦs show round to

elliptical shaped cells with a significantly lower TPE-AF intensity (Fig. 3d). Of nine cells with a TPE-FLIM M1 MΦ signature, eight cells stained positive for CD68, and all CD68-positive cells had a TPE-FLIM M1 MΦ signature. As for M2 MΦs, all cells with a TPE-FLIM M2 MΦ signature (12 of 14) were CD163-positive, and all CD163-positive cells had a TPE-FLIM M2 MΦ signature.

TPE-FLIM visualises human skin M1 and M2 MΦs in vivo

Next, we used TPE-FLIM to assess the skin of 25 healthy individuals *in vivo,* and we identified and further characterised 35 and 25 MΦs with a M1 and M2 TPE-FLIM signature, respectively. *In vivo*, similar to biopsy sections, M1 and M2 MΦs were located in the papillary and reticular dermis at >80 µm depth (Fig. 4) and showed a density of >100 MΦs/mm² (Figs. 1c, 1d). M1 MΦs fell into three distinct groups and were either flat and spindle shaped (Fig. 4a), slightly dendritic (Fig. 4b) or large and intervascular (Fig. 4c). M2 MΦs, in human skin *in vivo,* were round and moderately dendritic (Fig. 4d), and they had a higher TPE-AF intensity *in vivo* compared to the ECM, as previously reported *in vitro*(Malissen et al., 2014; Njoroge et al., 2001).

The TPE-FLIM parameters of *in vivo* M1 MΦs were in agreement with those of *in vitro* monocyte-derived and dermal M1 MΦs and *ex vivo* M1 MΦs (Fig. 4e, Table 1). M2 MΦs *in vivo* have longer τ_m fluorescence lifetimes compared to *in vitro* and *ex vivo* experiments. Yet, the τ_1 and τ_2 were in agreement with *in vitro* PBMC-derived monocytes, and the size and morphological parameters were in line with what is expected in M2 MΦs. The 2D segmentation in Fig. S5 shows the distinction of M1 and M2 MΦs presented in Figs. 4a-d, and the phasor plot in Fig. 4f shows that M1 and M2 MΦs could be distinguished from each other and from other dermal cells and ECM.
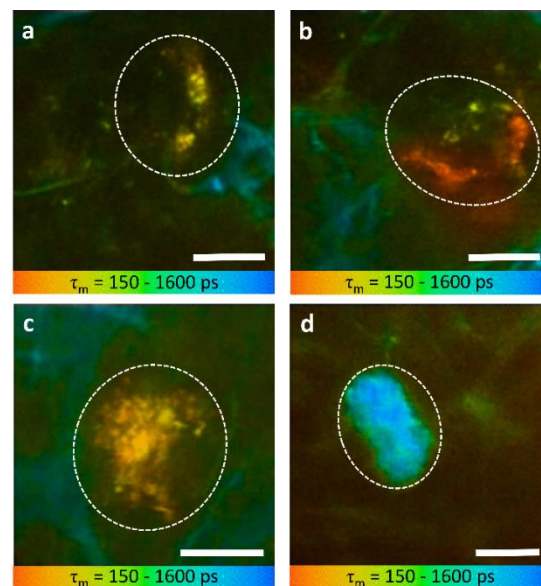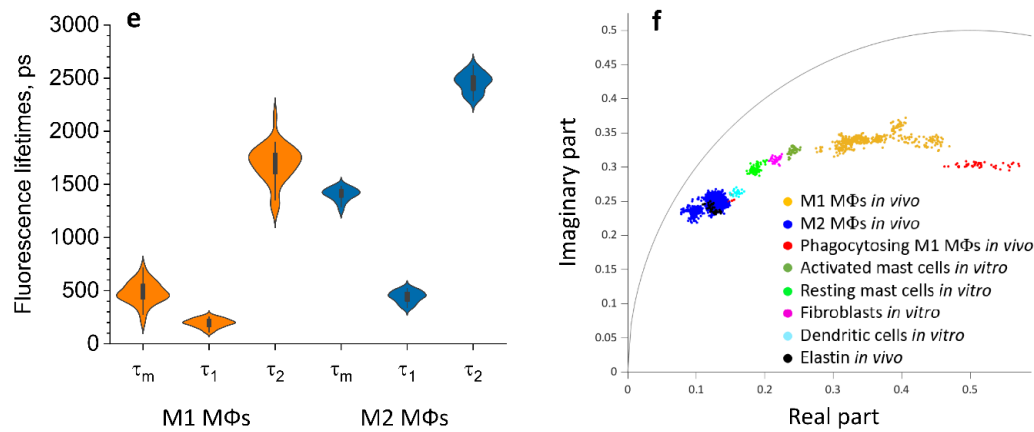
Figure 4. MΦs are visualised and categorised by TPE-FLIM signatures *in vivo*. TPE-FLIM *in vivo* images of potential perivascular flat spindle shaped M1 MΦ (a), of suspected slightly dendritic M1 MΦ in the depth 90 µm (b) large intervascular M1 MΦ with membrane extensions (c) and *in vivo* dermal cells resembling M2 MΦ were observed with a significantly longer mean fluorescence lifetime τ_m compared to M1 MΦs and less pronounced TPE-AF intensity (d), showing mean fluorescence lifetime τ_m in colour gradient from 150 to 1,600 ps. Scale bar: 10 µm. The histogram shows the distribution of TPE-FLIM parameters for *in vivo* MΦs (e). The boxplot represents 25–75% of the values. The phasor plot has a threshold at 0.9 of the maximum intensity and shows a summary of 12 M1, 2 phagocytosing M1 MΦs and 12 M2 MΦs *in vivo*, (f), where M1 MΦs are in orange and M2 MΦs in blue and phagocytosing M1 MΦs in red, the other dermal components are shown from *in vitro* measurements. The *in vivo* images (a–d) were recorded at 760 nm excitation wavelength, 50 mW laser power and 6.8 s acquisition time, in the depth of 80–100 µm on the volar forearm skin area of 25 healthy human subjects.

TPE-FLIM can distinguish resting from phagocytosing human skin M1 MΦs in vivo

Phagocytosing skin M1 MΦs are characterized by an increase in cell size(May and Machesky, 2001), enhanced vacuolization(Cheng et al., 2019) and a shift of TPE-FLIM parameters towards shorter fluorescence lifetime values(Yakimov et al., 2019), different from those of resting M1 and M2 MΦs. A dermal cell matching these criteria is visualized *in vivo* using TPE-FLIM and presented in Fig. 5. This cell is located in the reticular dermis, has an enlarged size (≈25 µm) and an oval shape, similar to the resting M1 MΦ in Fig. 4c, pronounced vacuole structure and short TPE-FLIM lifetime specific for phagocytosing M1 MΦ. Of 37 dermal M1 MΦs analysed, 2 showed phagocytosis, and both were located in the reticular dermis below 100 µm of depth.
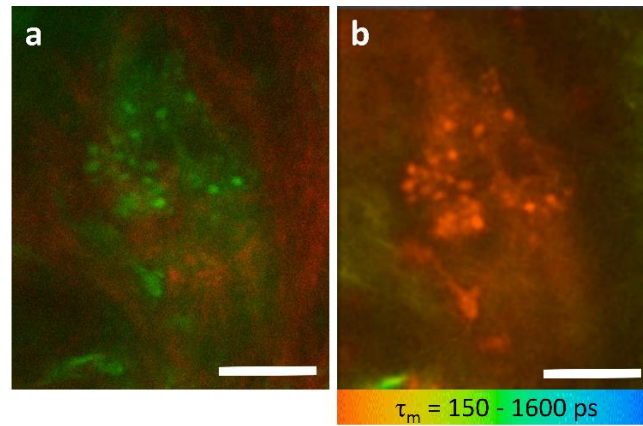
254

Figure 5. TPE-FLIM allows for visualization of phagocytosing M1 MΦs *in vivo*. Merged TPE-AF (green) and SHG (red) image of activated (phagocytosing) M1 MΦ measured *in vivo* in human papillary dermis at the depth 105 µm (a) and corresponding TPE-FLIM image (b), showing mean fluorescence lifetime τ_m in colour gradient from 150 to 1,600 ps. Scale bar: 10 µm. The images were recorded at 760 nm excitation wavelength, 50 mW laser power and 6.8 s acquisition time on the plantar forearm.

Classification algorithm to identify MΦs in the skin

To separate M1 and M2 MΦs from other dermal cells, we developed a classification algorithm, which used the decision tree (Fig. S6) and automatically classified MΦs based on their TPE-FLIM parameters and morphological features. The parameters of the decision tree were improved using hyperparameter optimization. The splitting method in the nodes of the decision tree classifier is chosen to be entropy impurity. To ensure the optimal quality of a split in the node of the decision tree, the following requirements had to be fulfilled: The minimal samples for a split is 2, the maximum depth of the tree is 9, and the samples had equal weight for the model classifying M1 and M2 MΦs. The ground truth was established by classification of *in vitro* and *ex vivo* MΦs with known phenotype resulting in 0.95±0.05 sensitivity and 0.97±0.06 specificity. When MΦs were classified as one group against other dermal cells, the sensitivity was 0.81±0.03 and the specificity was 0.81±0.03. Our algorithm also distinguished M1 MΦs from M2 MΦs and other cells, with a sensitivity of 0.88±0.04 and a specificity 0.89±0.03. For distinction of M2 MΦs from M1 MΦs and other cells, the sensitivity was 0.82±0.03 and the specificity was 0.90±0.03 (receiver operating characteristic is shown in Fig. S7.

Discussion

This is the first *in vivo* study to show that human skin MΦs can be distinguished from other dermal cells and quantified through visualization with label-free, completely non-invasive TPE-FLIM. This risk-free approach also allows for the identification of MΦ phenotypes, i.e. M1 and M2 MΦs, and for the characterization of their functional stage, i.e. resting vs phagocytosing M1 MΦs. Finally, TPE-FLIM can be used to implement sensitive and specific machine learning algorithms for MΦ detection in the skin.

Our initial work with CD-14 positive monocytes isolated from PBMC and then differentiated and polarised towards M1 (IFN-γ) and M2 (IL-4) MΦs was needed to establish their TPE-FLIM parameters. In fact, it showed that MΦs are fluorescence-active, and, more importantly, that their TPE-FLIM parameters are among the best differentiators

of of M1 (τ_m=479±106) and M2 (τ_m=1,185±170) MΦs. M1 MΦs are associated with a slightly higher TPE-AF intensity (Table 1), which is a prominent indicator for the metabolic stress of the cell on account of a shift in lifetimes by changing amounts of free and bound NAD(P)H (Al-Shabany et al., 2016) and generation of ROS in mitochondria, phagosomal vacuoles and the cell membrane (Datta et al., 2015). Additionally to NAD(P)H, autofluorescence of lipids and other cell compartments was recorded. TPE-AF intensity is a parameter with limitation due to the nonlinear imaging technique. There is no linear correlation between excitation and emission intensity, also it is reduced due to scattering and absorption in the skin. The longer fluorescence lifetime τ_2 in M2 MΦs is best explained by oxidative phosphorylation and the emergence of fluorophores caused by fatty acid oxidation(Viola et al., 2019). NAD(P)H fluorescence is ubiquitously present in cells and exhibits the continuum of lifetimes in the 360–3,400 ps range. Free NAD(P)H has a short lifetime of 360 ps. For bound NAD(P)H, longer lifetimes up to 2–4 ns have been reported(Alfonso-García et al., 2016). A higher ratio of bound to free NAD(P)H is associated with M2 MΦs resulting in longer TPE-FLIM parameters, while a lower ratio of bound to free NAD(P)H is associated with M1 MΦs resulting in faster TPE-AF decay(Blacker et al., 2014). Thus, a strong indicator for the MΦ polarization is the TPE-FLIM parameters of monocytes in between cohorts of MΦs.

Translation of our *in vitro* findings to MΦs isolated from human skin confirmed that the latter share the TPE-FLIM signatures of the former, with shorter τ_m in dermal M1 MΦs and longer τ_m in dermal M2 MΦs. The classification into M1 and M2 MΦs *in vitro* based on their distinct TPE-FLIM parameters was supported by their differences in size, morphology and internal vacuole structure. That the τ_1 lifetime of dermal M2 MΦs is longer than that of monocyte-derived M2 MΦs is most likely due to the use of different polarization agents. MΦ colony-stimulating factor (M-CSF) and IFNγ for M1 MΦs and MΦ colony-stimulating factor (M-CSF) and IL-4 for M2 MΦs were used in PBMC-derived MΦs and microenvironment effects like inflammatory signals, UV exposure (Kang et al., 1994) and immune responses (Theret et al., 2019) influencing MΦ functions, result in divergent fluorescence lifetimes (Zhang et al., 2014) (Table 1, Fig. 2d). The most important outcome of our work with dermal MΦs was the establishment of their phenotype-specific TPE-FLIM signatures, a prerequisite for our subsequent *in vivo* studies and for comparing skin MΦs and other dermal cells.

In fact, the use of the TPE-FLIM signatures of M1 and M2 MΦs clearly allowed to distinguish them from mast cells, dendritic cells, fibroblasts and neutrophils (Table 1, Fig. 4f) (Kröger et al., 2020). We controlled for this by independent markers. For example, MΦs exhibited a higher fluorescence intensity compared to other dermal cells. In addition, they were larger than dermal mast cells, and their morphology was clearly different from that of neutrophils and fibroblasts. Vacuoles, a defining feature of MΦs, were linked to MΦ TPE-FLIM parameters, whereas granules, which identify mast cells, were not. In short, dermal MΦs, in their TPE-FLIM profiles, do not superimpose with other dermal cells or structures. The only exception, a partial overlap between M2 MΦs and elastin, is not relevant for the visualization of the former, as they are readily distinguished from the latter based on their morphology.

To confirm that *ex vivo* TPE-FLIM overlap with TPE-FLIM signatures of M1 and M2 MΦs *in vitro*, we sequentially analyzed cells in skin biopsy cryosections with TPE-FLIM and conventional immunohistochemistry. Indeed, both approaches identified and distinguished matching MΦ populations, i.e. M1 and M2 MΦs, with strong fluorescence intensity and spindle shape appearance of M1 MΦs and lower fluorescence intensity and longer fluorescence decay in M2 MΦs (Fig. 3). Interestingly, M2 MΦs are often found in an area

of higher density of unknown dermal cells, presumably fibroblasts, compared to M1 MΦs. It is suspected that M2 MΦs in conjunction with collagen synthesizing fibroblasts are acting towards and aiding in dermal repair and regeneration. However, this approach also revealed some challenges that come with MΦ visualization by TPE-FLIM. For example, it was more difficult to visualise M2 MΦs than M1 MΦs in biopsies due to the high fluorescence intensity of elastin in dried tissue and other ECM components and a decreased signal-to-noise ratio. In Fig. 3d more CD163 positive M2 MΦs are visible compared to the corresponding TPE-FLIM image in Fig. 3c, which is due to previously mentioned challenges and the limited imaging plane of the two-photon tomograph (1.2–2.0 µm) compared to significantly thicker biopsy section (10 µm), which was stained in an entire depth and visualized by bright field microscopy. Importantly, immunohistochemistry confirmed our MΦ phenotype-specific TPE-FLIM signatures, and, in addition, confirmed that they distinguish MΦs from other dermal cells. Skin mast cells, for example, stained for tryptase, showed a distinct TPE-FLIM signature, confirming our recently reported findings on dermal mast cells *in vivo* (Kröger et al., 2020), and distinguished them from M1 and M2 MΦs (Fig. S8).

When we turned to the visualization of skin MΦs *in vivo*, we had to first develop a search strategy. Important considerations included the preferred localization of MΦs in the papillary and reticular dermis, the orientation of the focal plane parallel to the skin surface, and the need for maximal cellular cross-section visualization, which requires a high-resolution adjustment in depth to reconstruct an entire cell structure. The application of this search algorithm successfully visualised M1 and M2 MΦs in human skin *in vivo*. The *in vivo* TPE-FLIM parameters of M1 MΦs were in agreement with those observed *in vitro* and *ex vivo*. M2 MΦs *in vivo* were characterised by longer mean fluorescence lifetime τ_m compared to *in vitro* and *ex vivo* (Table 1), which can be explained by the influence of environment (Koo and Garg, 2019; Njoroge et al., 2001). MΦs measured *in vivo* differ from cells measured *in vitro* by their simplified microenvironment (Mosser and Edwards, 2008) with missing growth factors and cytokines (Melton et al., 2015) and an elevated level of nutrients, which leads to different polarization of MΦs and different contributions of fluorescence lifetimes. Membrane extensions were harder to detect *in vivo* due to the obscuring effect of the surrounding ECM. We also observed that TPE-FLIM parameters in the same MΦs can vary depending on their cellular substructures, e.g. the nucleus, vacuoles, cytoplasm, or membrane (Figs. 4a–d). The phasor plot shows the relative position of the categories of MΦs and other cells. Furthermore, it shows the contributions of long and short fluorescence lifetimes and their discrepancies (Table 1) are due to the computational method and the harmonics at the repetition frequency of 80 MHz. Further investigations are needed to clarify how the location, morphology, and function of M1 and M2 MΦs influence their TPE-FLIM parameters and TPE-AF intensity *in vivo*. Such studies should also investigate the reasons for the differences in TPE-FLIM parameters between M1 and M2 MΦs, which may include differences in their metabolic pathways. M1 MΦs, for example, rely on NADH oxidase and production of ROS, which is linked to short fluorescence lifetimes of under 250 ps and mitochondrial fission. M2 MΦs, on the other hand, rely on oxidative phosphorylation and fatty acid oxidation, together with mitochondrial fusion (Ramond et al., 2019; Swindle et al., 2002; Xu et al., 2016).

The ability to visualise M1 and M2 MΦs by TPE-FLIM *in vivo* also makes it possible to explore how and why MΦs' morphology, location and functions are linked. When activated, the cytoskeletal structure and cellular appearance of MΦs change, and this may also affect their TPE-FLIM parameters. M1 MΦs are elongated, with a dense actin network along the cortex. M2 MΦs are more spherical with more randomly distributed actin (Porcheray et al., 2005; Vogel et al., 2014; Zhang et al., 2014) (Figs. 4b and 4d). Actin reorganization in M1

and M2 MΦ polarization and activation lead to bigger filament bundles of the actin cytoskeleton, which reduces cell plasticity (Colin-York et al., 2019; Pergola et al., 2017). As reported by Daphne and coworkers (Vogel et al., 2014), MΦ migration in the skin depends on their polarization. M1 MΦs, due to changes in actin cytoskeleton, migrate less far than M2 MΦs. Our TPE-FLIM findings confirm this, as we detected M1 MΦs via their high fluorescence and short autofluorescence lifetimes primarily in close proximity to blood capillaries. The irregular appearance of M1 MΦ detected by TPE-FLIM is likely a consequence of polarization-specific changes of the cellular cytoskeleton (McWhorter et al., 2013). The only morphological feature observed in both, M1 and M2 populations of MΦs, is that they are moderately dendritic, possibly because such MΦs are in the process of polarization, prior to cytoskeletal changes (Sica and Mantovani, 2012), or because polarization in MΦs is reversible polarizing (Sica and Mantovani, 2012; Yuan et al., 2017). Future studies should characterise the influence of cytoskeletal changes on TPE-FLIM parameters in detail and use TPE-FLIM to assess the impact of age, gender, and disease on the ratio, localization and function of M1 and M2 MΦs in the skin (Fukui et al., 2018).

During phagocytosis, the generation of ROS by NAD(P)H oxidase leads to the highest degree of metabolic stress observed in M1 MΦs besides apoptosis (Dupré-Crochet et al., 2013; Shirshin et al., 2019), and ROS localization in vacuoles in phagocytosing M1 MΦs as a bactericidal mechanism (Dupré-Crochet et al., 2013; Myers et al., 2003). This is why phagocytosing M1 MΦs change their TPE-FLIM lifetimes towards shorter values and their vacuoles become visible as localised bright spots, which makes their *in vivo* detection possible (Fig. 5b, Table 1) (Cannon and Swanson, 1992). TPE-FLIM allowed for the detection of phagocytosing M1 MΦs but cannot detect what they phagocytised. No internal structure was visible in TPE-FLIM images.

The construction of the feature vector and the resulting hyperparameter optimised decision tree model (Fig. S6) yielded proficient results for the automatised classification of M1 and M2 MΦs, demonstrating that M1 and M2 MΦs can be separated from each other and other cells in the skin with high accuracy, i.e. sensitivity and specificity, without need of additional staining using a supervised machine learning approach. The accuracy of this approach can be improved further, by the introduction of a depth-adjusted cell size and refined cell shape parameters and by increasing the number of *in vivo* MΦs integrated into the algorithm and training data set.

Materials and Methods

Two-photon excited fluorescence lifetime imaging (TPE-FLIM)

For imaging of human MΦs, a two-photon tomograph (Dermainspect, JenLab GmbH, Jena, Germany), equipped with a tuneable femtosecond Ti:sapphire laser (Mai Tai XF, Spectra Physics, USA, 710–920 nm, 100 fs pulses at a repetition rate of 80 MHz), was used at 3–5 mW for measurements of cells *in vitro* and skin biopsy sections *ex vivo*, as well as human dermis *in vivo* at 40–50 mW. The excitation wavelength was set to 760 nm, and a 410–680 nm band pass filter was used to detect two-photon excited autofluorescence (TPE-AF), whereas a 375–385 nm band pass filter was used to detect the second harmonic generation (SHG) signals. The axial and lateral resolution was approximately 1.2–2.0 and 0.5 µm, respectively(Breunig et al., 2013). The penetration depth covers the entire papillary dermis (Darvin et al., 2014; König, 2008; Kröger et al., 2020).

Fluorescence decay of a specimen was recorded and analysed in the SPCImage 8.0 software (Becker&Hickl, Berlin, Germany). TPE-FLIM data were fitted with a bi-exponential decay function. The TPE-AF intensity threshold was chosen depending on the signal-to-noise ratio, minimizing noise in the region of interest. The shift of the signal in relation to the instrument response function (IRF) was compensated. The typical IRF value was <100 ps. The TPE-AF decay curves were averaged over the central pixel of the region of interest and the 48 closest square neighbouring pixels (binning = 3), resulting in a number of detected photons for each fluorescence decay curve larger than 5,000. The TPE-AF decay parameters, decay lifetimes (τ_1 and τ_2) and amplitudes (a_1 and a_2), were used for the evaluation of the fluorescence lifetime distributions and 2D segmentation(Shirshin et al., 2017). The analysed parameters were the mean lifetime, defined as $\tau_m=(a_1\tau_1+a_2\tau_2)/(a_1+a_2)$ and the ratios τ_2/τ_1, a_1/a_2 and $(a_1-a_2)/(a_1+a_2)$, which were used for 2D segmentation analysis. The TPE-FLIM data were also analysed and represented as phasor plots, that are based on the transformation of the fluorescence decay data in the frequency domain, whereas the decay is described as amplitude and phase values of the first Fourier component(Digman et al., 2008). The phasor plots' x-axis is described by the cosine of the phase value multiplied by the amplitude, the y-axis represents the sine of the phase value multiplied with the amplitude(Lakner et al., 2017; Shirshin et al., 2019). The position of the mean lifetime is on the secant from τ_1 and τ_2, the distance to the circle is given by the proportion of a_1 and a_2. The TPE-FLIM data were normalised to the maximum intensity and the threshold of 70% was set when analysing the phasor plots.

Ethical considerations and study conduct

Volunteers for intravital imaging provided written informed consent before participation. Skin samples taken from periocular skin surgery for MΦ preparation and all human skin investigated in this study were used after written informed consent was obtained. Positive votes for the experiments have been obtained from the ethics committee of the Charité – Universitätsmedizin Berlin (EA1/078/18, EA4/193/18, EA1/141/12), which were conducted according to the Declaration of Helsinki (59th WMA General Assembly, Seoul, October 2008).

Study subjects

25 healthy volunteers (12 males and 13 females, 24–65 years old, skin type I–III according to Fitzpatrick classification(Fitzpatrick, 1988)) with asymptomatic volar forearm skin without preexisting health conditions were randomly selected for non-invasive *in vivo* measurements in the papillary dermis using TPE-FLIM. Visually impairing hair was removed with a scissor prior to measurements. The oil immersion objective of the microscope was connected to the skin via a 150 µm thick, 18 mm diameter cover glass (VWR, Darmstadt, Germany) with a ≈10 µL distilled water droplet between cover glass and skin. The volunteers were screened between October 2018 and November 2020.

Investigation of human dermal MΦs in vitro

Human dermal MΦs were prepared from periocular tissue(Botting et al., 2017). Human periocular skin was digested in 2.4 U/ml dispase type II (Roche, Basel, Switzerland) at 4 °C for 12 hours. The dermis was minced with scissors after removal of the epidermis and further digested in PBS containing Ca^{2+} and Mg^{2+} (Gibco, Carlsbad, CA, USA) supplemented with 1% Pen/Strep, 5% FCS, 5 mM $MgSO_4$, 10 µg/ml DNaseI (Roche, Basel,

Switzerland), 2.5 µg/ml amphothericin (Biochrom, Berlin, Germany,) 1.5 mg/ml collagenase type II (Worthington Biochemical Corp., Lakewood, NJ, USA) and 0.75 mg/ml H-3506 hyaluronidase (Sigma-Aldrich, St. Louis, MO, USA) at 37 °C in a water bath with agitation for 60 min. The cell suspension was filtered using 300 µm and 40 µm stainless steel sieves (Retsch, Haan, Germany). Centrifugation at $300 \times$ g for 15 min at 4 °C was applied next. The digestion cycle was repeated once. MΦs were isolated by Pan Monocyte Isolation Kit (Miltenyi, Bergisch Gladbach Germany) after washing in PBS w/o Ca^{2+} and Mg^{2+} (Gibco, Carlsbad, CA, USA), and kept in basal Iscove's medium supplemented with 1% Pen/Strep, 10% FCS, 1% non-essential amino acids, 226 µM α-monothioglycerol (all Gibco, Carlsbad, CA, USA). For long-term cultures, after 24 h recombinant human IL-4 (20 ng/ml) and hSCF (100 ng/ml) (both Peprotech, Rocky Hill, NJ, USA) were added. Purity of MΦ cultures was routinely checked to be >85%(Nielsen et al., 2020). For imaging, cells were used after 3 days in medium, washed twice with PBS before seeding on 18 mm diameter microscope cover glass (VWR, Darmstadt, Germany) for imaging in PBS containing Ca^{2+} (Gibco, Carlsbad, CA, USA) at room temperature.

Investigation of peripheral blood monocytes in vitro

Peripheral blood monocytes were isolated from human blood using 15 ml Ficoll-Paque (VWR, Darmstadt, Germany) centrifugation gradient. Centrifugation was performed at $1,000 \times$ g for 1 minute, with added 9 ml heparin and filled to 50 ml with PBS. Centrifugation was then repeated at 1,000 g for 10 minutes, discarding the upper plasma layer and collecting the PBMC layer. The cells were washed twice with PBS and centrifuged at 350 $\times$ g for 10 minutes. The supernatant was discarded and cultured in 5 ml basal Iscove's medium supplemented with 1% Pen/Strep, 10% FCS (Biochtrom, Berlin, Germany) and subsequently incubated at 37 °C and 5% CO_2 for 2 h before seeded and imaged on an 18 mm diameter microscope cover glass (VWR, Darmstadt, Germany) in PBS containing Ca^{2+} (Gibco, Carlsbad, CA, USA) at room temperature.

Investigation of MΦs differentiated from peripheral blood monocytes in vitro

MΦs were differentiated from peripheral blood monocytes and polarised into M1 (IFNγ)-like state with MΦ colony-stimulating factor (M-CSF) and IFNγ and M2 (IL-4)-like state with MΦ colony-stimulating factor (M-CSF) and IL-4. For further stimulation, cells were incubated with LPS at 37 °C for 24 hours prior to imaging.

Investigation of dendritic cells in vitro

CD14 positive peripheral blood mononuclear cells were used to differentiate dendritic cells by washing in PBS and centrifuging at $350 \times$ g for 10 minutes twice. 5 ml RPMI medium, supplemented with 1% Pen/Strep and 1% FCS (Biochtrom, Berlin, Germany), was added. Tryptan Blue (Sigma-Aldrich, St. Louis, MO, USA) was used for counting the cells in a hemocytometer, seeded at 2.0×10^6 cells/ml and incubated for 2 hours at 37 °C under 5% CO_2. Non-attached cells and the supernatant were discarded. Adding 500 µl basal Iscove's medium to the cells supplemented with 1% Pen/Strep, 1% glutamine, 5% HSA, (all Gibco, Carlsbad, CA, USA) 100 ng/ml IL-4, 100 ng/ml GM-CSF (both Peprotech, Rocky Hill, NJ, USA) with medium change every second day for 6 days at 37 °C. For TPE-FLIM imaging the cells were seeded on 18 mm diameter microscope cover glass (VWR, Darmstadt, Germany) in PBS containing Ca^{2+} at room temperature.

Preparation and cryo-sectioning of human skin for combined TPE-FLIM and histomorphometric analysis

Thirteen human skin biopsy cryo-sections were prepared and measured using the TPE-FLIM method to acquire TPE-FLIM parameters of suspected M1 and M2 MΦs. The skin biopsies were obtained from abdominal reduction surgery of four female patients (31, 33, 40 and 44 y. o., skin type II according to Fitzpatrick classification(Fitzpatrick, 1988)). Punch biopsies of 6 mm diameter were obtained, frozen and stored at -80 °C before cryo-sectioning. Vertical histological cryo-sections of 10 µm thickness were prepared on a cryostat (Microm Cryo-Star HM 560, MICROM International GmbH, Walldorf, Germany) after embedding in a cryo-medium (Tissue Freezing Medium, Leica Biosystems Richmond Inc., Richmond, IL, USA) and placed on 18 mm diameter microscope cover glasses (VWR, Darmstadt, Germany). The anatomical condition of the biopsies was continuously examined using a transmission microscope (Olympus IX 50, Olympus K.K., Shinjuku, Tokyo, Japan).

Using TPE-FLIM, cryo-sections were searched for cells with MΦ-specific TPE-FLIM parameters and the corresponding TPE-FLIM images of suspected MΦs were recorded. To prove the measured cells are MΦs, the skin biopsies were labeled by irradiating a squared area of 28 µm×28 µm located near the suspected MΦs with a Ti:sapphire laser (Mai Tai XF, Spectra Physics, USA, 100 fs pulses at a repetition rate of 80 MHz) at a maximal power of 50 mW at 760 nm for 3 seconds. All incubations were performed at room temperature unless otherwise stated. In brief, sections were fixed for 10 min in cold acetone (-20 °C) and rinsed in TBS (Agilent, Santa Clara, CA, USA). For staining of MΦs, the MΦ-specific anti-CD68 (clone ab955) (Abcam, Cambridge, UK), Recombinant Anti-CD163 antibody [EPR14643-36] (clone ab189915) (Abcam, Cambridge, UK) were used to account for M1 and M2 MΦ phenotypes, respectively. Slides were rinsed three times with TBS, and endogenous peroxidase was blocked with 3% H_2O_2 in TBS for 5 min followed by incubation with anti-mouse EnVision+ labelled polymer (Agilent Technologies, Santa Clara, USA) for 30 min. Slides were rinsed in TBS as before and incubated with AEC substrate-chromogen (Agilent Technologies, Santa Clara, USA) for 10 min. Nuclei were counterstained with Mayer's hemalum solution (Merck, Darmstadt, Germany). Stained MΦs have a brown-red color, which enables to visually distinguish them from other cells and the ECM. After the staining procedure, target MΦs and squared labels of the skin sections were identified by light microscopy and overlaid with TPE-FLIM images matching an appropriate magnification and image orientations.

Specifically, CD68-stained M1 MΦs were counted in the papillary dermis region in each biopsy, and an average of 209±25 cells/mm² for the papillary dermis and an average of 140±76 cells/mm² for the reticular dermis for a 10 µm deep cryo-section was observed (Fig. 1c). The density of the CD163 stained M2 MΦs was an average of 242±126 cells/mm² for the papillary dermis and an average of 107±60 cells/mm² for the reticular dermis for a 10 µm deep cryo-section (Fig. 1d).

The MΦs search algorithm we then used was similar to that recently presented by our group for the identification of resting and activated mast cells in the papillary dermis(Kröger et al., 2020) and included the following steps: First, the papillary dermis (≈60–100 µm depth for volar forearm) was explored for fluorescent spots of 10–15 µm in size with irregular shape and a membrane extension having bright spots of about 1–3 µm. The TPE-FLIM parameters of the suspected bright areas were measured and matched those of M1 and M2 MΦs obtained *in vitro* and *ex vivo*.

To prove that the TPE-FLIM parameters of other dermal cells, which have detectable TPE-AF intensity, namely, mast cells and dendritic cells do not match or superimpose with TPE-

569 FLIM parameters of MΦs, negative control measurements were performed. The procedure
570 was similar as described for the verification of MΦs in skin biopsies using specific
571 immunofluorescence, but six human skin cryo-sections were stained for the presence of
572 mast cells and two for dendritic cells.

573 Staining of mast cells was done by blocking with serum-free protein followed by incubation
574 for 1 h with anti-tryptase antibody (clone AA1) diluted 1:1,000 in antibody diluent (all
575 Agilent, Santa Clara, CA, USA). For staining of dendritic cells, anti-CD11c antibody (clone
576 B-Ly6) (BD Biosciences, Franklin Lakes, NJ, USA) was used after fixing the cryo-section
577 for 10 min in cold acetone (-20 °C) and rinsing with TBS.

578 ### *Statistical analysis and classification algorithm*

579 Matlab R2016a (MathWorks, Natick, MA, USA) was applied for descriptive statistics of all
580 TPE-FLIM data. All results are indicated as mean±standard deviation. Differences between
581 distributions were compared using the non-parametric Kolmogorov-Smirnov test with a
582 significance level of α=0.05. The decision tree classifier was modelled using Scikit-learn
583 0.22 in a Python 3.7 environment (Python Software Foundation, Delaware, USA). A
584 randomised training set, consisting of 50% of the complete data set, was used for training
585 and validating the test set 10,000 times. The true positive- and true negative rates were
586 calculated from the confusion matrix and describe the quality of the classification and
587 indicate type I and type II errors. For the decision tree(Breiman et al., 1984), the TPE-FLIM
588 parameters τ_1, τ_2, τ_m, τ_1/τ_2, a_1, a_2, a_1/a_2, $(a_1-a_2)/(a_1+a_2)$, TPE-AF intensity, cell shape, and
589 decay curve were used for each cell measured *in vitro*, *ex vivo*, and *in* and
590 hyperparametrically optimized(Yang and Shami, 2020). The feature vector was constructed
591 as follows: 1 (shape (circular form)) + 1 (normalised TPE-AF intensity of cell normalised
592 by the cell's area and excitation power) + 256 (fluorescence decay curve) + 8 (TPE-FLIM
593 parameters obtained after bi-exponential approximation of the decay curve), in total, 266
594 values. The MΦ size was not included in the feature vector for the classification model, as
595 MΦs *in vivo* could have slightly different dimensions from those measured *in vitro* (in cell
596 cultures) and *ex vivo* (in biopsies), caused by obscuring effects of surrounding dermal tissue.
597 Here, 1 represents circular and 0 non-circular shape. The lifetimes calculated from the bi-
598 exponential decay model were averaged over the whole cell, and the fluorescence intensity
599 was normalised by optical power and averaged the pixel of interest and the 48 neighbouring
600 square pixel.

601 In total, 110 MΦs *in vitro*, 20 MΦs *ex vivo*, 70 MΦs *in vivo* (for M1/M2 ratio see Table 1),
602 59 mast cells *in vitro*, 17 mast cells *ex vivo*, 82 mast cells *in vivo*, 14 dendritic cells *in vitro*,
603 6 fibroblasts *in vitro* and 21 neutrophils *in vitro* were used as input for the model (399 cells
604 in total). Given data vectors from $x_i \in R^n$, i=1,…,l and a label vector $y_i \in R^l$, where a
605 decision tree recursively separates the data into two classes with the mode m represented
606 as Q. For each node a split $\theta = (j, t_m)$ decided with the feature j and the threshold t_m. The
607 node split the data into subsets $Q_{left}(\theta)$ and $Q_{right}(\theta)$

608 $$Q_{left}(\theta) = (x,y)|x_j <= t_m$$

609 $$Q_{right}(\theta) = Q\backslash Q_{right}(\theta)$$

610 The impurity was calculated by the impurity function $H()$ at the mode m

611 $$G(Q,\theta) = {}^{n_{left}}/_{N_m} H(Q_{left}(\theta)) + {}^{n_{right}}/_{N_m} H(Q_{right}(\theta))$$

612   With the parameters for minimised impurities the subsets were recourse until $N_m = 1$.

613   The returns values of the classification were 0 for M1 MΦs, 1 for M2 MΦs and 2 for other
614   dermal cells, 0 for MΦs and 1 for other dermal cells for node m in the region R_m and N_m
615   observation, the proportion of class k observations in node m is $p_{mk} = 1/N_m \sum_{x_i \in R_m} I(y_i = k)$.
616   k).

617   Receiver operating characteristic (ROC)-curves served as a tool to determine the diagnostic
618   abilities of the method, where the true positive rate was plotted against the false positive
619   rate of the respective outcomes for both the categorization of MΦs against other dermal
620   cells and M1 MΦs and M2 MΦs against other dermal cells.

621
622
623
624
625
626
627
628
629
630
631
632
633
634
635
636
637
638
639
640
641
642
643
644
645
646
647
648
649
650
651
652
653
654
655
656
657
658
659
660
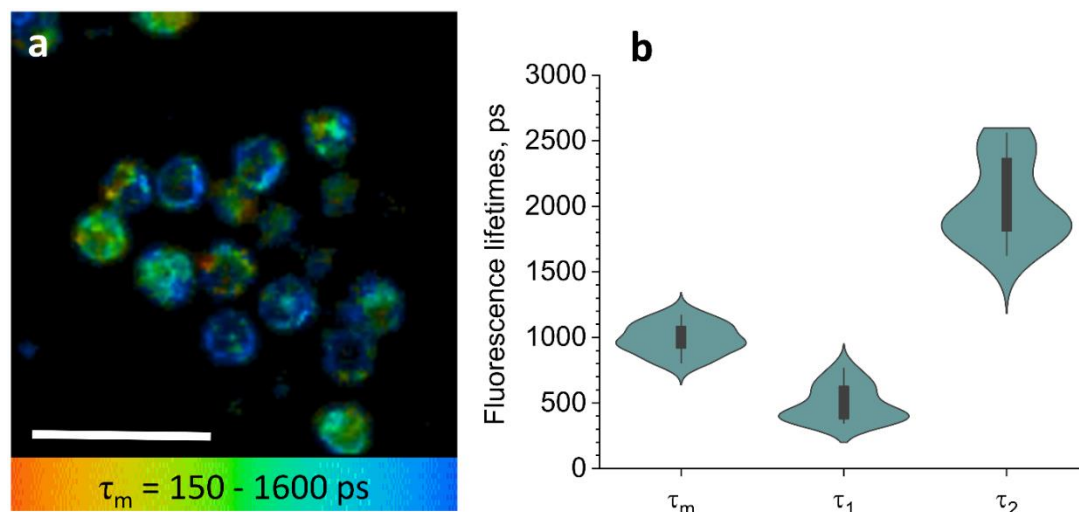
Supplementary Materials

Fig. S1. TPE-FLIM visualisation of PBMC and histogram of TPE-FLIM parameter. TPE-FLIM τ_m images (mean fluorescence lifetime τ_m in the 150–1,600 ps range) of PBMC (a) Scale bar: 10 µm. The distribution of TPE-FLIM parameters τ_1, τ_2 and τ_m for PBMC ($n=15$) (f).
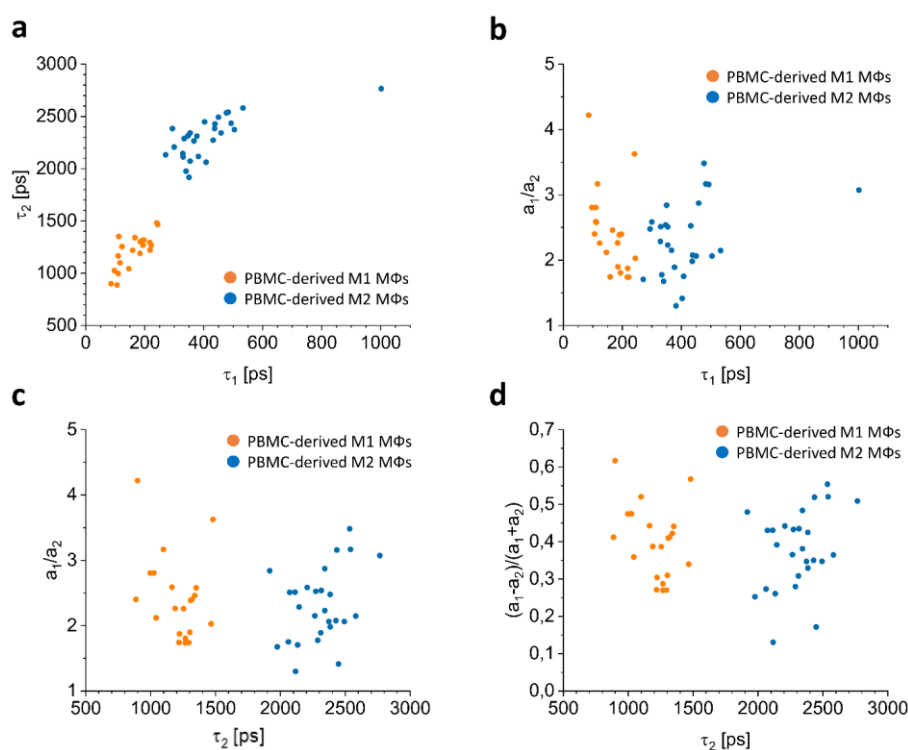

Fig. S2. *In vitro* **2D segmentation for MΦs from PBMC.** 2D segmentation of the $\tau_1(\tau_2)$ (a), $\tau_1(a_1/a_2)$ (b), $\tau_2(a_1/a_2)$ (c) and $\tau_2((a_1-a_2)/(a_1+a_2))$ (d) TPE-FLIM parameters of the M1 MΦs (orange circles) and M2 MΦs (blue circles) measured *in vitro*.
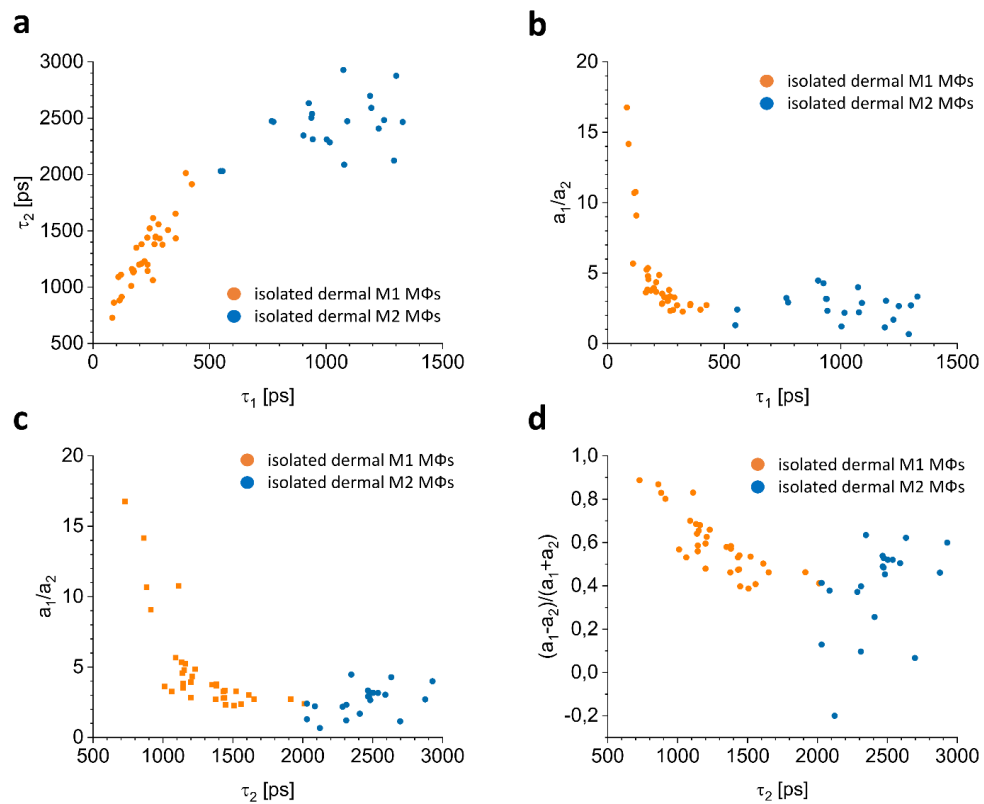
Fig. S3. *In vitro* segmentation for MΦs from dermal tissue. 2D segmentation of the $\tau_1(\tau_2)$ (a), $\tau_1(a_1/a_2)$ (b), $\tau_2(a_1/a_2)$ (c) and $\tau_2((a_1-a_2)/(a_1+a_2))$ (d) TPE-FLIM parameters of the M1 MΦs (orange circles) and M2 MΦs (blue circles) measured *in vitro*.
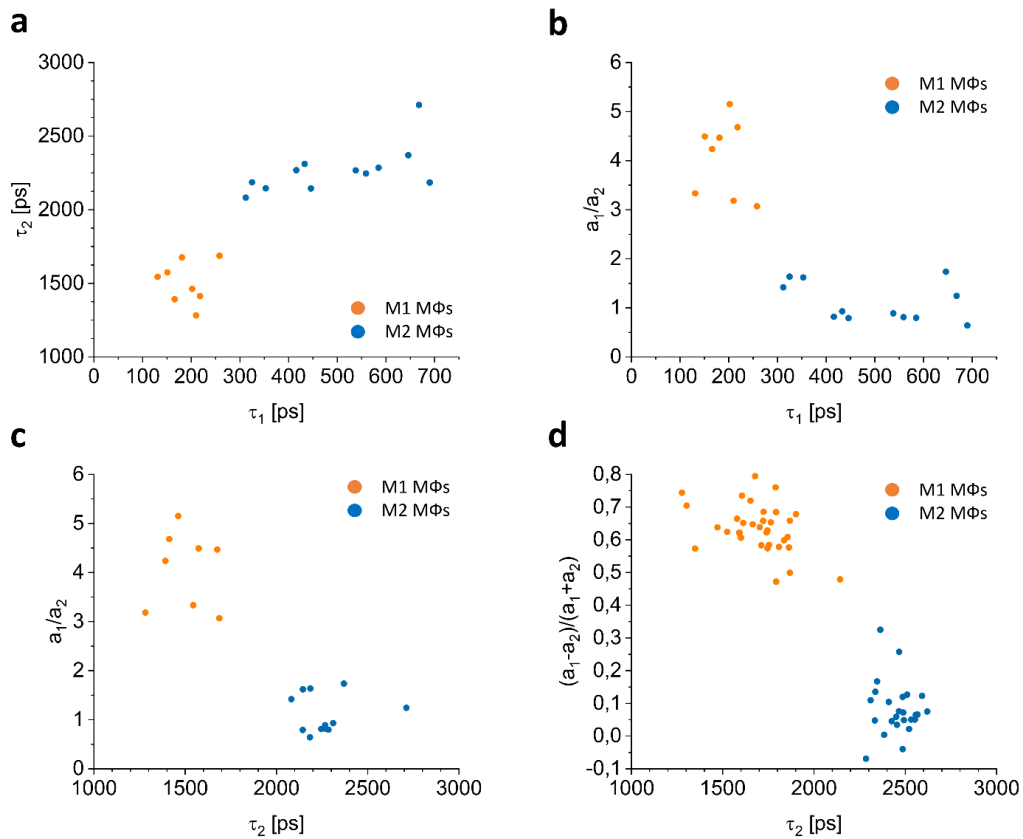
680

Fig. S4. *Ex vivo* segmentation for MΦs from skin biopsies. 2D segmentation of the $\tau_1(\tau_2)$ (a), $\tau_1(a_1/a_2)$ (b), $\tau_2(a_1/a_2)$ (c) and $\tau_2((a_1-a_2)/(a_1+a_2))$ (d) TPE-FLIM parameters of the M1 MΦs (orange circles) and M2 MΦs (blue circles) measured *ex vivo*.
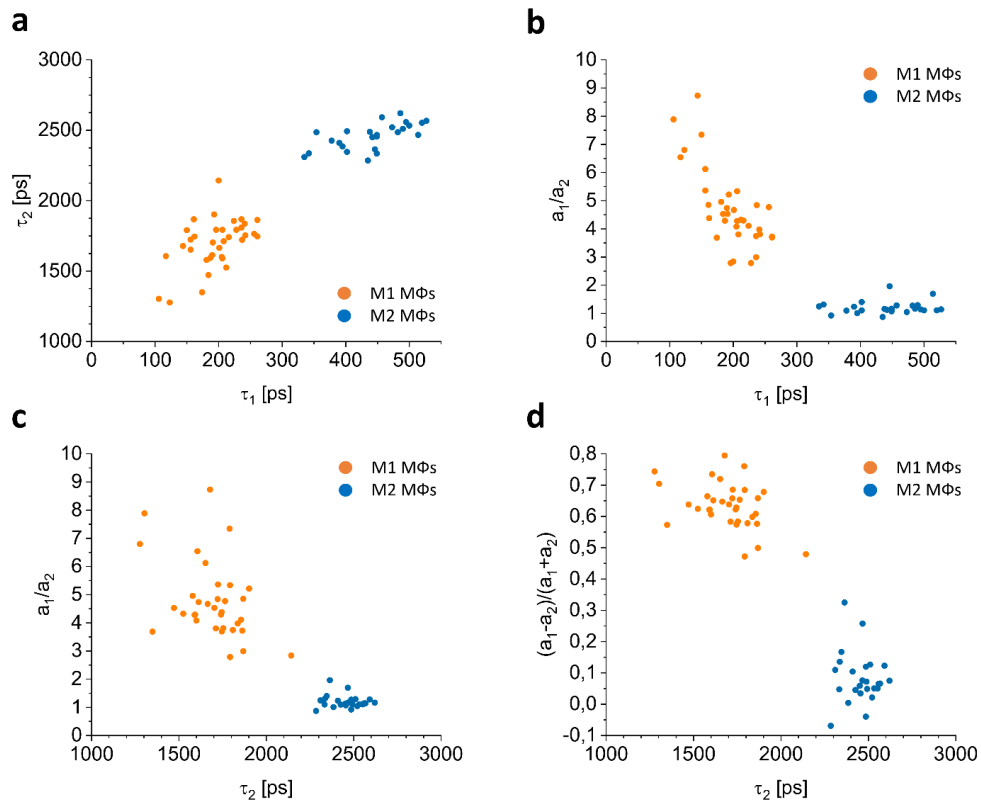
684

685

Fig. S5. *In vivo* segmentation for MΦs in human skin. 2D segmentation of the $\tau_1(\tau_2)$ (a), $\tau_1(a_1/a_2)$ (b), $\tau_2(a_1/a_2)$ (c) and $\tau_2((a_1-a_2)/(a_1+a_2))$ (d) TPE-FLIM parameters of the M1 MΦs (orange circles) and M2 MΦs (blue circles) measured *in vitro*.
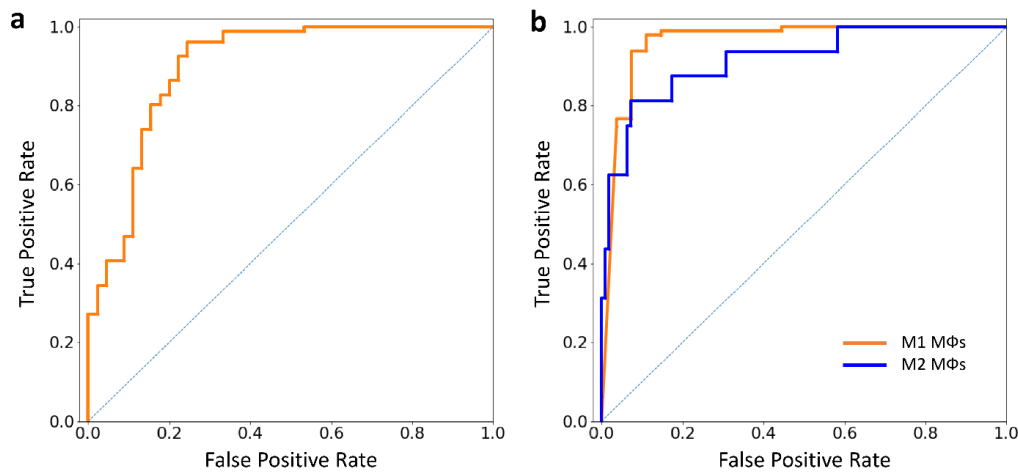
689

690

Fig. S6. Decision tree model. Decision tree model for classification of M1 and M2 MΦs with the parameters entropy impurity, minimal samples for split is 2, maximum depth of the tree is 9, and the samples had equal weight. The text of the decision tree is readable when zoomed in.

Fig. S7. ROC curves of decision tree models. ROC curves of false positive to false negative rates for classification of MΦs versus other dermal cells (a) and for classification of M1 MΦs (orange line) versus M2 MΦs and other dermal cells and for classification of M2 MΦs (blue line) versus M1 MΦs and other dermal cells (b) generated from the decision tree classifier (Fig. S6).
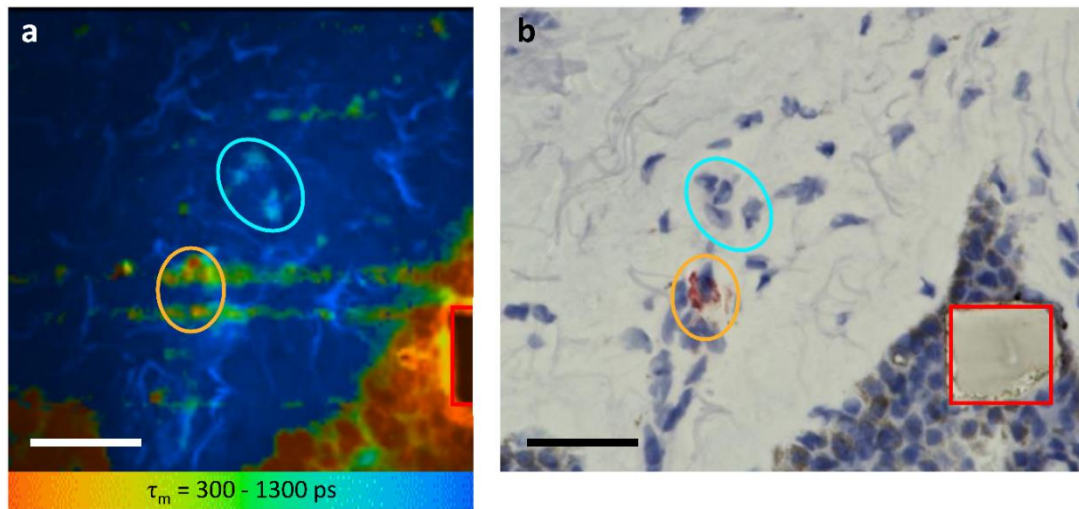

Fig. S8. Mast cell-specific staining with tryptase *ex vivo* – negative control. Side by side comparison of TPE-FLIM image (average lifetime τ_m in the 300–1,300 ps range) (a) and corresponding light microscopic image after staining of human skin biopsy cryo-sections for MCs (b). Laser power is 3 mW, excitation at 760 nm. The MCs are marked with orange ellipses, suspected MΦs are marked with blue ellipses, and the laser burned squares (28×28 µm^2) used for labeling are marked in red. Images have been rotated and zoomed to match the same orientation and size. Scale bar: 30 µm.

References

Al-Shabany AJ, Moody AJ, Foey AD, Billington RA. 2016. Intracellular NAD+ levels are associated with LPS-induced TNF- release in pro-inflammatory macrophages. *Biosci Rep* **36**:e00301–e00301. doi:10.1042/bsr20150247

Alfonso-García A, Smith TD, Datta R, Luu TU, Gratton E, Potma EO, Liu WF. 2016. Label-free identification of macrophage phenotype by fluorescence lifetime imaging microscopy. *J Biomed Opt* **21**:046005. doi:10.1117/1.jbo.21.4.046005

Benoit M, Desnues B, Mege J-L. 2008. Macrophage Polarization in Bacterial Infections. *J Immunol* **181**:3733–3739. doi:10.4049/jimmunol.181.6.3733

Blacker TS, Mann ZF, Gale JE, Ziegler M, Bain AJ, Szabadkai G, Duchen MR. 2014. Separating NADH and NADPH fluorescence in live cells and tissues using FLIM. *Nat Commun* **5**:3936. doi:10.1038/ncomms4936

Botting RA, Bertram KM, Baharlou H, Sandgren KJ, Fletcher J, Rhodes JW, Rana H, Plasto TM, Wang XM, Lim JJK, Barnouti L, Kohout MP, Papadopoulos T, Merten S, Olbourne N, Cunningham AL, Haniffa M, Harman AN. 2017. Phenotypic and functional consequences of different isolation protocols on skin mononuclear phagocytes. *J Leukoc Biol* **101**:1393–1403. doi:10.1189/jlb.4a1116-496r

Breiman L, Friedman JH, Olshen RA, Stone CJ. 1984. Classification and regression trees, The Wadsworth statistics/probability series. Monterey, CA: Wadsworth & Brooks/Cole Advanced Books & Software.

Breunig HG, Weinigel M, Bückle R, Kellner-Höfer M, Lademann J, Darvin ME, Sterry W, König K. 2013. Clinical coherent anti-Stokes Raman scattering and multiphoton tomography of human skin with a femtosecond laser and photonic crystal fiber. *Laser Phys Lett* **10**:025604. doi:10.1088/1612-2011/10/2/025604

Cannon GJ, Swanson JA. 1992. The macrophage capacity for phagocytosis. *J Cell Sci* **101**:907–913. doi:10.1242/jcs.101.4.907

Cheng J, Zhang Q, Fan S, Zhang A, Liu B, Hong Y, Guo J, Cui D, Song J. 2019. The vacuolization of macrophages induced by large amounts of inorganic nanoparticle uptake to enhance the immune response. *Nanoscale* **11**:22849–22859. doi:10.1039/c9nr08261a

Colin-York H, Li D, Korobchevskaya K, Chang VT, Betzig E, Eggeling C, Fritzsche M. 2019. Cytoskeletal actin patterns shape mast cell activation. *Commun Biol* **2**:1–12. doi:10.1038/s42003-019-0322-9

Darvin ME, Richter H, Ahlberg S, Haag SF, Meinke MC, Le Quintrec D, Doucet O, Lademann J. 2014. Influence of sun exposure on the cutaneous collagen/elastin fibers and carotenoids: negative effects can be reduced by application of sunscreen. *J Biophotonics* **7**:735–743. doi:10.1002/jbio.201300171

Datta R, Alfonso-Garciá A, Cinco R, Gratton E. 2015. Fluorescence lifetime imaging of endogenous biomarker of oxidative stress. *Sci Rep* **5**:1–10. doi:10.1038/srep09848

Digman MA, Caiolfa VR, Zamai M, Gratton E. 2008. The phasor approach to fluorescence lifetime imaging analysis. *Biophys J* **94**:L14-6. doi:10.1529/biophysj.107.120154

Dong B, Almassalha LM, Stypula-Cyrus Y, Urban BE, Chandler JE, Nguyen T-Q, Sun C, Zhang HF, Backman V. 2016. Superresolution intrinsic fluorescence imaging of chromatin utilizing native, unmodified nucleic acids for contrast. *Proc Natl Acad Sci* **113**:9716–9721. doi:10.1073/pnas.1602202113

Dupré-Crochet S, Erard M, Nüβe O. 2013. ROS production in phagocytes: why, when, and where? *J Leukoc Biol* **94**:657–670. doi:10.1189/jlb.1012544

Duque GA, Descoteaux A. 2014. Macrophage cytokines: Involvement in immunity and infectious diseases. *Front Immunol* **5**:1–12. doi:10.3389/fimmu.2014.00491

Elhelu MA. 1983. The role of macrophages in immunology. *J Natl Med Assoc* **75**:314–7.

Estandarte AK, Botchway S, Lynch C, Yusuf M, Robinson I. 2016. The use of DAPI fluorescence

768   lifetime imaging for investigating chromatin condensation in human chromosomes. *Sci Rep*
769   **6**:1–12. doi:10.1038/srep31417
770 Ferrer MF, Thomas P, Ortiz AOL, Errasti AE, Charo N, Romanowski V, Gorgojo J, Rodriguez
771   ME, Silva EAC, Gómez RM. 2019. Junin virus triggers macrophage activation and modulates
772   polarization according to viral strain pathogenicity. *Front Immunol* **10**:1–12.
773   doi:10.3389/fimmu.2019.02499
774 Fitzpatrick TB. 1988. The Validity and Practicality of Sun-Reactive Skin Types I Through VI. *Arch*
775   *Dermatol* **124**:869–871.
776 Forman HJ, Torres M. 2001. Redox signaling in macrophages. *Mol Aspects Med* **22**:189–216.
777   doi:10.1016/S0098-2997(01)00010-3
778 Fukui S, Iwamoto N, Takatani A, Igawa T, Shimizu T, Umeda M, Nishino A, Horai Y, Hirai Y,
779   Koga T, Kawashiri SY, Tamai M, Ichinose K, Nakamura H, Origuchi T, Masuyama R, Kosai
780   K, Yanagihara K, Kawakami A. 2018. M1 and M2 Monocytes in rheumatoid arthritis: A
781   contribution of imbalance of M1/M2 monocytes to osteoclastogenesis. *Front Immunol* **8**:1–
782   10. doi:10.3389/fimmu.2017.01958
783 Furukawa S, Moriyama M, Miyake K, Nakashima H, Tanaka A, Maehara T, Iizuka-Koga M,
784   Tsuboi H, Hayashida JN, Ishiguro N, Yamauchi M, Sumida T, Nakamura S. 2017. Interleukin-
785   33 produced by M2 macrophages and other immune cells contributes to Th2 immune reaction
786   of IgG4-related disease. *Sci Rep* **7**:1–10. doi:10.1038/srep42413
787 Geissmann F, Manz M, Jung S, Sieweke M, Merad M, Ley K. 2010. Development of monocytes,
788   macrophages and dendritic cells. *Science (80-)* **327**:565–661.
789   doi:10.1126/science.1178331.Development
790 Gordon S, Taylor PR. 2005. Monocyte and macrophage heterogeneity. *Nat Rev Immunol* **5**:953–
791   964. doi:10.1038/nri1733
792 Heaster TM, Heaton AR, Sondel PM, Skala MC. 2021. Intravital Metabolic Autofluorescence
793   Imaging Captures Macrophage Heterogeneity Across Normal and Cancerous Tissue. *Front*
794   *Bioeng Biotechnol* **9**:1–10. doi:10.3389/fbioe.2021.644648
795 Kang K, Hammerberg C, Meunier L, Cooper KD. 1994. CD11b+ macrophages that infiltrate human
796   epidermis after in vivo ultraviolet exposure potently produce IL-10 and represent the major
797   secretory source of epidermal IL-10 protein. *J Immunol* **153**:5256–5264.
798 König K. 2008. Clinical multiphoton tomography. *J Biophotonics* **1**:13–23.
799   doi:10.1002/jbio.200710022
800 Koo S jie, Garg NJ. 2019. Metabolic programming of macrophage functions and pathogens control.
801   *Redox Biol* **24**:101198. doi:10.1016/j.redox.2019.101198
802 Kröger M, Scheffel J, Nikolaev V V, Shirshin EA, Siebenhaar F, Schleusener J, Lademann J,
803   Maurer M, Darvin ME. 2020. In vivo non-invasive staining-free visualization of dermal mast
804   cells in healthy, allergy and mastocytosis humans using two-photon fluorescence lifetime
805   imaging. *Sci Rep* **10**:14930. doi:10.1038/s41598-020-71901-2
806 Lakner PH, Monaghan MG, Möller Y, Olayioye MA, Schenke-Layland K. 2017. Applying phasor
807   approach analysis of multiphoton FLIM measurements to probe the metabolic activity of three-
808   dimensional in vitro cell culture models. *Sci Rep* **7**. doi:10.1038/srep42730
809 Li Y, Liu TM. 2018. Discovering macrophage functions using in Vivo optical imaging techniques.
810   *Front Immunol* **9**:1–20. doi:10.3389/fimmu.2018.00502
811 Malissen B, Tamoutounour S, Henri S. 2014. The origins and functions of dendritic cells and
812   macrophages in the skin. *Nat Rev Immunol* **14**:417–428. doi:10.1038/nri3683
813 Malmgaard L, Melchjorsen J, Bowie AG, Mogensen SC, Paludan SR. 2004. Viral Activation of
814   Macrophages through TLR-Dependent and -Independent Pathways. *J Immunol* **173**:6890–
815   6898. doi:10.4049/jimmunol.173.11.6890
816 May RC, Machesky LM. 2001. Phagocytosis and the actin cytoskeleton. *J Cell Sci* **114**:1061–1077.
817 McWhorter FY, Wang T, Nguyen P, Chung T, Liu WF. 2013. Modulation of macrophage

818   phenotype by cell shape. *Proc Natl Acad Sci U S A* **110**:17253–17258.
819   doi:10.1073/pnas.1308887110

820 Melton DW, McManus LM, Gelfond JAL, Shireman PK. 2015. Temporal phenotypic features
821   distinguish polarized macrophages in vitro. *Autoimmunity* **48**:161–176.
822   doi:10.3109/08916934.2015.1027816

823 Mendoza-Coronel E, Ortega E. 2017. Macrophage polarization modulates FcγR- and CD13-
824   mediated phagocytosis and reactive oxygen species production, independently of receptor
825   membrane expression. *Front Immunol* **8**. doi:10.3389/fimmu.2017.00303

826 Morhenn VB, Lemperle G, Gallo RL. 2002. Phagocytosis of different particulate dermal filler
827   substances by human macrophages and skin cells. *Dermatologic Surg* **28**:484–490.
828   doi:10.1046/j.1524-4725.2002.01273.x

829 Mosser DM, Edwards JP. 2008. Exploring the full spectrum of macrophage activation. *Nat Rev*
830   *Immunol* **8**:958–969. doi:10.1038/nri2448

831 Murray PJ, Allen JE, Biswas SK, Fisher EA, Gilroy DW, Goerdt S, Gordon S, Hamilton JA,
832   Ivashkiv LB, Lawrence T, Locati M, Mantovani A, Martinez FO, Mege JL, Mosser DM,
833   Natoli G, Saeij JP, Schultze JL, Shirey KA, Sica A, Suttles J, Udalova I, vanGinderachter JA,
834   Vogel SN, Wynn TA. 2014. Macrophage Activation and Polarization: Nomenclature and
835   Experimental Guidelines. *Immunity* **41**:14–20. doi:10.1016/j.immuni.2014.06.008

836 Myers JT, Tsang AW, Swanson JA. 2003. Localized Reactive Oxygen and Nitrogen Intermediates
837   Inhibit Escape of Listeria monocytogenes from Vacuoles in Activated Macrophages. *J*
838   *Immunol* **171**:5447–5453. doi:10.4049/jimmunol.171.10.5447

839 Nielsen MC, Andersen MN, Møller HJ. 2020. Monocyte isolation techniques significantly impact
840   the phenotype of both isolated monocytes and derived macrophages in vitro. *Immunology*
841   **159**:63–74. doi:10.1111/imm.13125

842 Njoroge JM, Mitchell LB, Centola M, Kastner D, Raffeld M, Miller JL. 2001. Characterization of
843   viable autofluorescent macrophages among cultured peripheral blood mononuclear cells.
844   *Cytometry* **44**:38–44. doi:10.1002/1097-0320(20010501)44:1<38::AID-
845   CYTO1080>3.0.CO;2-T

846 Pergola C, Schubert K, Pace S, Ziereisen J, Nikels F, Scherer O, Hüttel S, Zahler S, Vollmar AM,
847   Weinigel C, Rummler S, Müller R, Raasch M, Mosig A, Koeberle A, Werz O. 2017.
848   Modulation of actin dynamics as potential macrophage subtype-targeting anti-tumour strategy.
849   *Sci Rep* **7**:1–12. doi:10.1038/srep41434

850 Ploeger DT, Hosper NA, Schipper M, Koerts JA, De Rond S, Bank RA. 2013. Cell plasticity in
851   wound healing: Paracrine factors of M1/ M2 polarized macrophages influence the
852   phenotypical state of dermal fibroblasts. *Cell Commun Signal* **11**:1–17. doi:10.1186/1478-
853   811X-11-29

854 Porcheray F, Viaud S, Rimaniol AC, Léone C, Samah B, Dereuddre-Bosquet N, Dormont D, Gras
855   G. 2005. Macrophage activation switching: An asset for the resolution of inflammation. *Clin*
856   *Exp Immunol* **142**:481–489. doi:10.1111/j.1365-2249.2005.02934.x

857 Ramond E, Jamet A, Coureuil M, Charbit A. 2019. Pivotal role of mitochondria in macrophage
858   response to bacterial pathogens. *Front Immunol* **10**:1–11. doi:10.3389/fimmu.2019.02461

859 Remmerie A, Scott CL. 2018. Macrophages and lipid metabolism. *Cell Immunol* **330**:27–42.
860   doi:10.1016/j.cellimm.2018.01.020

861 Rendra E, Riabov V, Mossel DM, Sevastyanova T, Harmsen MC, Kzhyshkowska J. 2019. Reactive
862   oxygen species (ROS) in macrophage activation and function in diabetes. *Immunobiology*
863   **224**:242–253. doi:10.1016/j.imbio.2018.11.010

864 Ryter A. 1985. Relationship between ultrastructure and specific functions of macrophages. *Comp*
865   *Immunol Microbiol Infect Dis* **8**:119–133. doi:10.1016/0147-9571(85)90039-6

866 Schmid MA, Harris E. 2014. Monocyte Recruitment to the Dermis and Differentiation to Dendritic
867   Cells Increases the Targets for Dengue Virus Replication. *PLoS Pathog* **10**.

868   doi:10.1371/journal.ppat.1004541

869 Shirshin EA, Gurfinkel YI, Priezzhev A V., Fadeev V V., Lademann J, Darvin ME. 2017. Two-
870   photon autofluorescence lifetime imaging of human skin papillary dermis in vivo: Assessment
871   of blood capillaries and structural proteins localization. *Sci Rep* **7**:1171. doi:10.1038/s41598-
872   017-01238-w

873 Shirshin EA, Yakimov BP, Darvin ME, Omelyanenko NP, Rodionov SA, Gurfinkel YI, Lademann
874   J, Fadeev V V., Priezzhev A V. 2019. Label-Free Multiphoton Microscopy: The Origin of
875   Fluorophores and Capabilities for Analyzing Biochemical Processes. *Biochem* **84**:69–88.
876   doi:10.1134/s0006297919140050

877 Sica A, Mantovani A. 2012. Macrophage plasticity and polarization: in vivo veritas. *J Clin Invest*
878   **122**:787–795. doi:10.1172/JCI59643DS1

879 Swindle EJ, Hunt JA, Coleman JW. 2002. A Comparison of Reactive Oxygen Species Generation
880   by Rat Peritoneal Macrophages and Mast Cells Using the Highly Sensitive Real-Time
881   Chemiluminescent Probe Pholasin: Inhibition of Antigen-Induced Mast Cell Degranulation by
882   Macrophage-Derived Hydrogen Pero. *J Immunol* **169**:5866–5873.
883   doi:10.4049/jimmunol.169.10.5866

884 Szulczewski JM, Inman DR, Entenberg D, Ponik SM, Aguirre-Ghiso J, Castracane J, Condeelis J,
885   Eliceiri KW, Keely PJ. 2016. In Vivo Visualization of Stromal Macrophages via label-free
886   FLIM-based metabolite imaging. *Sci Rep* **6**:1–9. doi:10.1038/srep25086

887 Theret M, Mounier R, Rossi F. 2019. The origins and non-canonical functions of macrophages in
888   development and regeneration. *Dev* **146**:1–14. doi:10.1242/dev.156000

889 Viola A, Munari F, Sánchez-Rodríguez R, Scolaro T, Castegna A. 2019. The metabolic signature
890   of macrophage responses. *Front Immunol* **10**:1–16. doi:10.3389/fimmu.2019.01462

891 Vogel DYS, Heijnen PDAM, Breur M, de Vries HE, Tool ATJ, Amor S, Dijkstra CD. 2014.
892   Macrophages migrate in an activation-dependent manner to chemokines involved in
893   neuroinflammation. *J Neuroinflammation* **11**:1–11. doi:10.1186/1742-2094-11-23

894 Walsh AJ, Mueller KP, Tweed K, Jones I, Walsh CM, Piscopo NJ, Niemi NM, Pagliarini DJ, Saha
895   K, Skala MC. 2021. Classification of T-cell activation via autofluorescence lifetime imaging.
896   *Nat Biomed Eng* **5**:77–88. doi:10.1038/s41551-020-0592-z

897 Weber-Matthiesen K, Sterry W. 1990. Organization of the monocyte/macrophage system of normal
898   human skin. *J Invest Dermatol* **95**:83–89. doi:10.1111/1523-1747.ep12874002

899 Xu Q, Choksi S, Qu J, Jang J, Choe M, Banfi B, Engelhardt JF, Liu ZG. 2016. NADPH oxidases
900   are essential for macrophage differentiation. *J Biol Chem* **291**:20030–20041.
901   doi:10.1074/jbc.M116.731216

902 Yakimov BP, Gogoleva MA, Semenov AN, Rodionov SA, Novoselova M V., Gayer A V., Kovalev
903   A V., Bernakevich AI, Fadeev V V., Armaganov AG, Drachev VP, Gorin DA, Darvin ME,
904   Shcheslavskiy VI, Budylin GS, Priezzhev A V., Shirshin EA. 2019. Label-free
905   characterization of white blood cells using fluorescence lifetime imaging and flow-cytometry:
906   molecular heterogeneity and erythrophagocytosis. *Biomed Opt Express* **10**:4220.
907   doi:10.1364/boe.10.004220

908 Yanez DA, Lacher RK, Vidyarthi A, Colegio OR. 2017. The role of macrophages in skin
909   homeostasis. *Pflugers Arch Eur J Physiol* **469**:455–463. doi:10.1007/s00424-017-1953-7

910 Yang L, Shami A. 2020. On hyperparameter optimization of machine learning algorithms: Theory
911   and practice. *Neurocomputing* **415**:295–316.
912   doi:https://doi.org/10.1016/j.neucom.2020.07.061

913 Yuan R, Li S, Geng H, Wang X, Guan Q, Li X, Ren C, Yuan X. 2017. Reversing the polarization
914   of tumor-associated macrophages inhibits tumor metastasis. *Int Immunopharmacol* **49**:30–37.
915   doi:10.1016/j.intimp.2017.05.014

916 Zhang XM, Lund H, Mia S, Parsa R, Harris RA. 2014. Adoptive transfer of cytokine-induced
917   immunomodulatory adult microglia attenuates experimental autoimmune encephalomyelitis

918   in DBA/1 mice. *Glia* **62**:804–817. doi:10.1002/glia.22643

919

920

921

922

923

924   **Acknowledgments**

925